Available online at www.sciencedirect.com
SCIENCE DIRECT
Intermetallics 14 (2006) 607–619
Intermetallics
www.elsevier.com/locate/intermet

The flow stress anomaly in Fe–43at%Al single crystals

U. Messerschmidt *, M. Bartsch, Ch. Dietzsch

Max Planck Institute of Microstructure Physics, D-06120 Halle/Saale, Germany

Received 24 January 2005; received in revised form 21 October 2005; accepted 24 October 2005
Available online 20 December 2005

Abstract

Fe–43at%Al single crystals were deformed in compression between room temperature and 700 °C. The strain rate sensitivity of the flow stress was measured by stress relaxation tests. The dislocation structure of the deformed samples was studied in a high-voltage transmission electron microscope. In addition, micro-tensile specimens were deformed in situ in this microscope to directly observe the dynamic behaviour of the dislocations. The specimens show a flow stress anomaly accompanied with an 'inverse' dependence of the strain rate sensitivity on the strain rate. Both the in situ experiments and the transmission electron micrographs of macroscopically deformed samples indicate the occurrence of climb at temperatures in and above the anomaly range. In the in situ experiments, viscously moving dislocations are straight and crystallographically oriented. The phenomena related to the flow stress anomaly are interpreted by the decomposition of the cores of dislocations with ⟨111⟩ Burgers vectors.

Keywords: A. Iron aluminides, based on FeAl; B. Plastic deformation mechanisms; D. Defects: dislocation geometry and arrangement; Electron microscopy, F. transmission; F. Mechanical testing

1. Introduction

Within a certain temperature range, many intermetallic alloys show a flow stress anomaly, i.e. an increasing flow stress with increasing temperature. This is a desired property to achieve high strength at high temperatures. As discussed in [1], a number of models were established to explain the flow stress anomaly in B2 ordered FeAl crystals. They include

- cross slip of dislocations with ⟨111⟩ Burgers vectors from their {110} slip plane onto {112} planes where they get pinned, by analogy with Ni_3Al [2],
- local decomposition of dislocations with ⟨111⟩ Burgers vectors into partials with ⟨001⟩ and ⟨110⟩ Burgers vectors which impedes the dislocation motion [3],
- localized climb of the antiphase boundary-coupled partials of the dislocations with ⟨111⟩ Burgers vectors [4] according to a model originally proposed to explain the flow stress anomaly in β brass [5], and
- hardening owing to the high concentration of thermal vacancies at the temperatures of the flow stress anomaly [1] after the observation that the anomaly occurs only in specimens in which the high excess vacancy concentration originating from the crystal preparation is annealed out by long-time annealing at relatively low temperatures [6].

In FeAl, the situation is additionally complicated since there is a transition of the dominating Burgers vector from ⟨111⟩ to ⟨100⟩ [7,8] just at the temperature of the flow stress peak which may cause the anomaly [9]. However, it was shown by rapid quenching after deformation that dislocations with ⟨111⟩ Burgers vectors dominate during deformation at the high strain rate of $5\times10^{-2}\,s^{-1}$ even at a high temperature of about 650 °C [10]. Similarly, it was observed that the deformation at the peak temperature of 550 °C started by dislocations with ⟨111⟩ Burgers vectors and such with ⟨100⟩ Burgers vectors appeared only after a few per cent of plastic strain [11]. The ⟨100⟩ dislocations are supposed to be formed by decomposition of ⟨111⟩ dislocations although in this study no indications were found of this process.

In some materials, the anomaly is due to diffusion processes in the dislocation cores (e.g. [12]) with a dynamic behaviour like the Cottrell effect [13]. The process is also named dynamic strain ageing. It causes a friction stress σ^* which depends on the dislocation velocity (or strain rate $\dot{\varepsilon}$) and the temperature T as drawn schematically in Fig. 1. At low dislocation velocities or strain rates in range A, a point defect cloud can easily diffuse

* Corresponding author. Fax: +49 345 5511 223.
E-mail address: um@mpi-halle.de (U. Messerschmidt).

0966-9795/$ - see front matter © 2005 Elsevier Ltd. All rights reserved.
doi:10.1016/j.intermet.2005.10.009

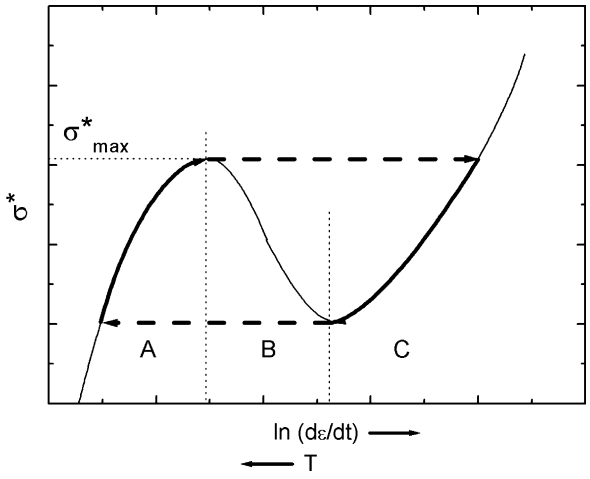

Fig. 1. Schematic diagram of the dependence of a friction stress on the strain rate or temperature according to a Cottrell effect type interaction between dislocations and point defects.

with the dislocation causing a low flow stress contribution. It increases with increasing dislocation velocity up to a maximum value σ^*_{max}. At higher strain rates in range B the cloud cannot follow the dislocation anymore so that the stress contribution decreases again. In range C, the point defects may act as fixed non-diffusing obstacles to the dislocation motion resulting in the normal increase of the stress contribution with increasing velocity. If the abscissa in Fig. 1 is read as a (reverse) temperature axis, the maximum of the curve explains the flow stress anomaly. The slope of the curve corresponds to the strain rate sensitivity of the flow stress $r = d\sigma/d\ln\dot{\varepsilon}$. In the stable range A, r is positive but decreases with increasing strain rate down to zero at the maximum stress. This behaviour is opposite to the normal behaviour in the stable range C where r increases with increasing $\dot{\varepsilon}$. This is called here an 'inverse' dependence of r on $\dot{\varepsilon}$. It was shown in studies of stress relaxation curves that the 'inverse' behaviour appears just in the ranges of a flow stress anomaly in several intermetallic alloys [14,15]. In the intermediate range B, r is negative.

The Cottrell effect type interaction between diffusing point defects and dislocations leads to a particular dynamic behaviour of the latter. In range A of the curve, the dislocation motion is viscous, in contrast to a very jerky athermal motion in pure metals at high temperatures. Deformation in range B may be unstable because of the negative strain rate sensitivity r of the flow stress σ (Portevin–LeChâtelier (PLC) effect [16,17], see e.g. [18]). The inverse dependence of r on $\dot{\varepsilon}$, mentioned above, is just connected with the dynamic dislocation behaviour typical of Cottrell effect type interactions, i.e. a viscous or unstable mode of dislocation motion at high temperatures [14,15].

It is the aim of the present paper to look whether the flow stress anomaly in FeAl single crystals has also characteristics of the Cottrell effect type interaction between dislocations and point defects as in some other intermetallic materials, or not. For this aim,

- macroscopic deformation experiments were performed including stress relaxation tests to study the dependence of the strain rate sensitivity r on the strain rate $\dot{\varepsilon}$,
- in situ straining experiments were carried out at different temperatures in a high-voltage electron microscope (HVEM) to observe the dynamic behaviour of dislocations, and
- the dislocation microstructures of the macroscopically deformed specimens were observed in the HVEM to assure that dislocations of a single slip system are operating in the whole range of the flow stress anomaly. The HVEM has the advantage that relatively thick specimens can be studied revealing the three-dimensional dislocation structure.

2. Experimental

The starting material of this study, a large Fe-43at%Al single crystal, was thankfully obtained from Oak Ridge National Laboratory. It was annealed at 400 °C for 1 week followed by slow cooling to room temperature to anneal out the excess point defects originating from crystal growth. Specimens in size of about $2.5\times2.5\times6.5\ mm^3$ for compression experiments along a [753] axis with one $(13\ \overline{50}\ 53)$ side face about 10° off $(0\ \bar{1}\ 1)$ were cut by spark erosion, ground and carefully polished. The orientation favours single slip on the $(101)[11\bar{1}]$ slip system. Other slip systems with a reasonable orientation factor are listed in Table 1. The specimens were deformed in a single-screw testing machine under digital strain control resulting in a very high effective stiffness. Some specimens were deformed at a constant strain rate of $10^{-5}\ s^{-1}$ or $10^{-4}\ s^{-1}$. In several experiments, the strain rate was changed between 10^{-6}, 10^{-5}, 10^{-4}, and $[10^{-3}\ s^{-1}$ after strain intervals of fractions of a per cent to study the dependence of serrated flow on the strain rate. Some specimens were deformed by strain intervals of about 1% at different temperatures. The strain rate sensitivity $r = d\sigma/d\ln\dot{\varepsilon}$ of the flow stress was measured by stress relaxation tests. The logarithm of the relaxation rate was plotted as a function of the stress σ. In these relaxation curves, the strain rate sensitivity equals the reciprocal slope of the curve

$$r = d\sigma/d\ln(-\dot{\sigma}). \quad (1)$$

Specimens for transmission electron microscopy were cut by a wire saw either parallel to the (101) glide plane or parallel to the side face mentioned above. They were then dimpled and

Table 1
Orientation factors m_s of possible slip systems at [753] orientation of loading axis

Slip system	m_s
$(101)[11\bar{1}]$	0.44
$(011)[11\bar{1}]$	0.35
(101)[010]	0.42
(011)[100]	0.48
(010)[100]	0.42

polished by electrolytic jet polishing between platinum masks at 30 V and −35 °C in a solution of 100 ml perchloric acid and 7 g thiourea in 900 ml ethanol. Micro-tensile specimens for in situ straining experiments in the HVEM were prepared by similar methods using two-stage jet polishing with the same loading axis and a $(1\bar{2}1)$ foil normal. The experiments were performed in double-tilting room temperature or high-temperature straining stages [19,20]. The HVEM was operated at 1000 kV.

3. Results

3.1. Macroscopic deformation tests

Fig. 2 shows stress–strain curves at about 250, 550 and 650 °C with sections taken at the different strain rates indicated. The curves are either smooth or serrated depending on the temperature and the strain rate. The dependence of the amplitude of the serrations on these parameters is demonstrated in Fig. 3. Smooth deformation curves occur only at room temperature for strain rates above $10^{-6}\,s^{-1}$ and above about 550 °C for strain rates less than $10^{-3}\,s^{-1}$. The amplitude of the serrations scatters remarkably. It is almost independent of the strain rate and increases with increasing temperature. Below 550 °C, optical microscopy shows single slip on localized bands corresponding to the (101) primary slip plane and above that temperature traces belonging to the (011) plane.

The temperature dependence of the yield stress σ is plotted in Fig. 4. Strain rates of 10^{-5} and $10^{-4}\,s^{-1}$ are indicated by different symbols. The values are obtained by linear extrapolation of the work-hardening range onto zero plastic strain as outlined in Fig. 2a. Some data points labelled by open symbols do not correspond to the initial yield stress but are taken after some plastic strain followed by temperature changes. In these cases, the values are the sum of the initial yield stress and the stress differences due to the temperature changes. The curve in Fig. 4 consists of three ranges, a low-temperature range of a normal temperature dependence, i.e. with a slightly decreasing flow stress between room temperature and about 350 °C, a range of an anomalous increase between about 350 and 550 °C, and a high-temperature range above 550 °C with again a normal decrease of the flow stress. In this range, very strong yield points occur, as shown in Fig. 2c. Fig. 4 presents the lower yield points. The upper yield point of 342 MPa at 594 °C has almost the same value as the stress maximum at 550 °C. After the yield points, the work-hardening rate is very low.

The strain rate sensitivity was studied by stress relaxation tests. Some typical curves are presented in Fig. 5. They are quite straight or have the usual curvature towards the stress axis, corresponding to most obstacle mechanisms. Inside a very small range within the anomaly range of an increasing flow stress with increasing temperature (at 533 and 542 °C), the curves have a typical two-stage shape with a bending away from the stress axis. As outlined in Section 1, this 'inverse' curvature points at a mechanism with the dynamics of the Cottrell effect for the flow stress anomaly. Values of the strain

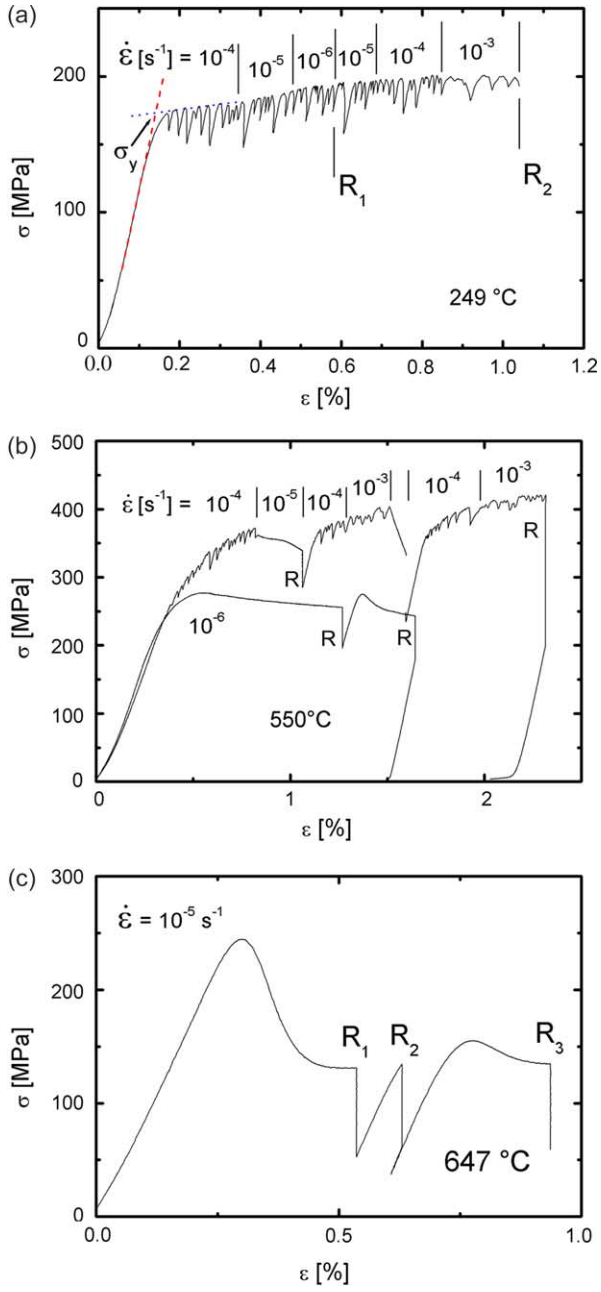

Fig. 2. Stress–strain curves at about 250 °C (a), 550 °C (b) and 650 °C (c) taken at the indicated strain rates. R_n are stress relaxation tests.

rate sensitivity r of the flow stress shown in Fig. 6 were evaluated from the slope of the stress relaxation curves at strain rates of 10^{-5} and $10^{-7}\,s^{-1}$. They are very small up to about 530 °C and show a maximum at about 600 °C, i.e. above the flow stress peak. In the anomaly range, the values measured at the strain rate of $10^{-7}\,s^{-1}$ are higher than those at $10^{-5}\,s^{-1}$, in agreement with the inverse curvature of the relaxation curves. In the high-temperature range, the behaviour is opposite as expected from the normal temperature dependence of the flow stress. Strain rate change experiments in a wide range of strain rates between 5×10^{-7} and $10^{-4}\,s^{-1}$ show zero strain rate sensitivity at room temperature, 250 and 533 °C.

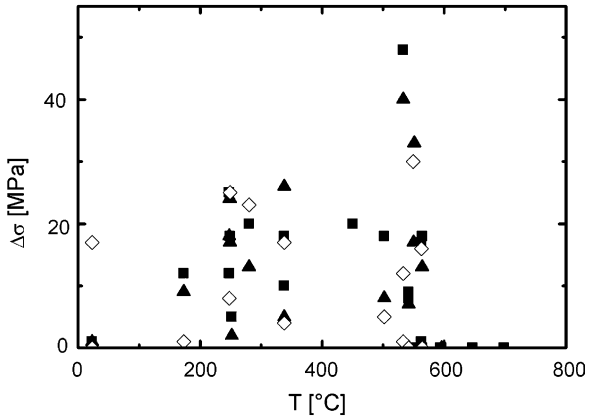

Fig. 3. Amplitude of stress serrations as a function of the deformation temperature. Triangles: strain rate $\dot{\varepsilon} = 10^{-4}$ s^{-1}, squares: $\dot{\varepsilon} = 10^{-5}$ s^{-1}, open diamonds: $\dot{\varepsilon} = 10^{-6}$ s^{-1},

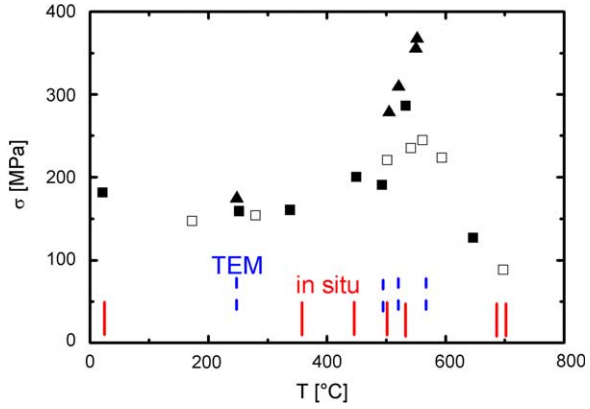

Fig. 4. Temperature dependence of the flow stress. Triangles: $\dot{\varepsilon} = 10^{-4}$ s^{-1}, squares: $\dot{\varepsilon} = 10^{-5}$ s^{-1}. Solid symbols indicate the initial flow stress of individual experiments. Open symbols mark flow stresses after temperature changes corrected for work hardening, see text. Dashed (blue) vertical lines indicate the temperatures of TEM studies of dislocation structures, (red) solid ones those of in situ straining experiments (for interpretation of the reference to colour in this legend, the reader is referred to the web version of this article.).

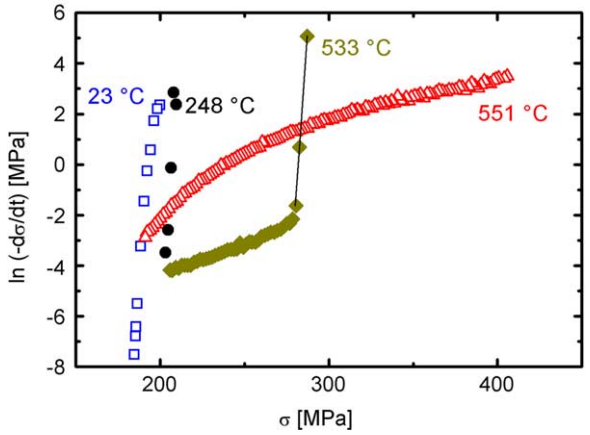

Fig. 5. Stress relaxation curves at different temperatures.

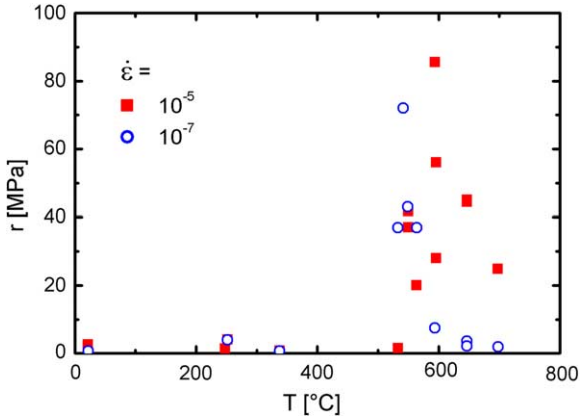

Fig. 6. Dependence of the strain rate sensitivity r measured from the slope of stress relaxation curves at strain rates of 10^{-5} and 10^{-7} s^{-1}.

3.2. Transmission electron microscopy of dislocation structures of deformed samples

As stated in Section 1, these studies were mainly performed to assure that the Burgers vector does not change in the temperature range of the flow stress anomaly. The Burgers vectors were determined by the $\mathbf{g}\cdot\mathbf{b}=0$ contrast extinction rule. The temperatures where dislocation structures were studied in the HVEM are labelled in Fig. 4 by dashed (blue) vertical marks. Fig. 7 presents the dislocation structure of a specimen deformed in the anomaly range at 521 °C in a foil cut parallel to the (13 $\overline{5}0$ 53) side face. At the operating **g** vector, the majority of dislocations in slip bands are visible. **t** is the trace of the (101) primary slip plane. Burgers vector analysis with a number of **g** vectors shows that the primary Burgers vector is $\mathbf{b} = [11\bar{1}]$. Its projection onto the image plane is parallel to the **g** vector. This and other examples verify that in

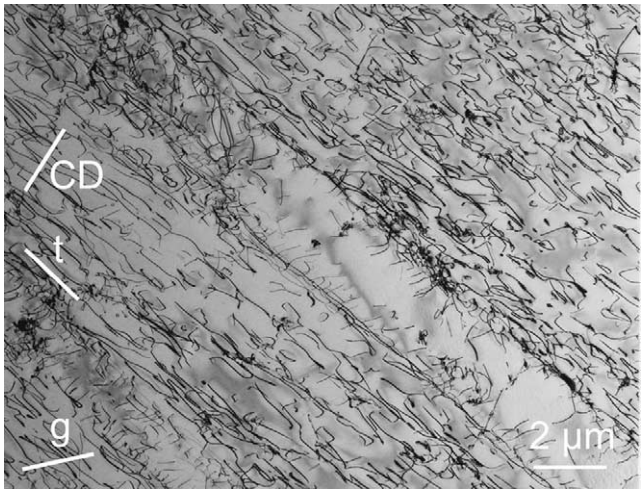

Fig. 7. Dislocation structure in a foil cut parallel to the (13 $\overline{5}0$ 53) side face of a sample deformed at 521 °C at a strain rate of 10^{-4} s^{-1} to a plastic strain of about 0.8%. Diffraction vector $\mathbf{g}=(200)$ near the pole $\mathbf{n}=[0\bar{1}1]$ **g** is also the projection of the Burgers vector $\mathbf{b}=[11\bar{1}]$ onto the image plane. $\mathbf{t}=[\bar{1}11]$ is the trace of the (101) main slip plane, $\mathbf{CD}=[744]$ is the projection of the compression direction onto the image plane.

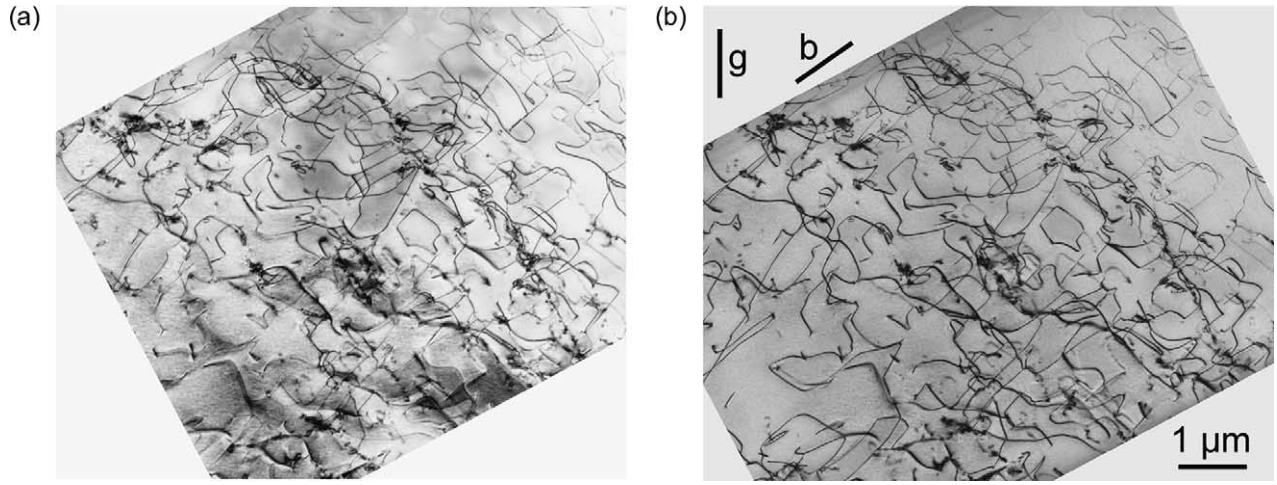

Fig. 8. Stereo image of a foil cut parallel to the primary (101) slip plane from the same deformation experiment as Fig. 7. $\mathbf{g}=(020)$ near $\mathbf{n}=[101]$, $\mathbf{b}=[11\bar{1}]$.

macroscopic experiments the ⟨111⟩ Burgers vectors dominate in the low-temperature and anomaly ranges. At the $[\bar{1}\bar{1}1]$ pole the dislocations are imaged as straight lines perpendicular to the (101) **g** vector, showing that they extend roughly on the primary (101) slip plane. The central region of Fig. 7, which is almost free of dislocations, borders two wide slip bands. The edges of these bands consist of relatively straight screw dislocations while in the interior of the bands dislocations with large edge components dominate.

Stereo image pairs of the same specimen region reveal that many dislocations are only roughly arranged on their slip planes. This is more clearly shown in the stereo pair of Fig. 8, taken of a foil cut parallel to the primary (101) slip plane. There are only very few segments which lie in the image plane. Most segments do not belong to the primary slip plane. Some are smoothly curved but others extend parallel to crystallographic directions. The latter is also obvious from the micrograph in Fig. 9 of a specimen deformed at 495 °C. Many dislocation lines exhibit an angular shape with a sharp edge. Two of them are indicated by an arrow. It will be discussed below that the edges are due to an elastic instability. If the overall orientation of a dislocation lies in the unstable range, the dislocation decomposes into stable segments as labelled by A.

In specimens deformed above the flow stress peak, dislocations with ⟨100⟩ Burgers vectors dominate. Thus, in macroscopic deformation experiments, the Burgers vector changes at the peak temperature from $[11\bar{1}]$ to ⟨100⟩, but this transition is not the cause of the anomalous increase of the flow stress. Also the dislocations with ⟨100⟩ Burgers vectors show preferential orientations and an elastic instability as demonstrated by the cross-sectional specimen in Fig. 10 (black arrows).

3.3. In situ straining experiments

The temperatures where in situ straining experiments were performed in the HVEM are indicated by full (red) vertical lines in Fig. 4. At room temperature, dislocation motion was observed in the plastic zone of a crack. Usually, $(10\bar{1})$ reflections were used at the $[1\bar{2}1]$ pole of the foil normal, where dislocations with [010] Burgers vectors are extinguished. Fig. 11 shows the dislocation structure during deformation. $\mathbf{b}_1$ and $\mathbf{b}_2$ mark the $[11\bar{1}]$ and $[\bar{1}11]$ Burgers vectors. Moving near screw dislocations with Burgers vector $\mathbf{b}_1$ are labelled by arrows. In the upper part of the figure, long dislocations of 30° character have developed. All dislocations bow out between cusps in the dislocation lines. The distances l

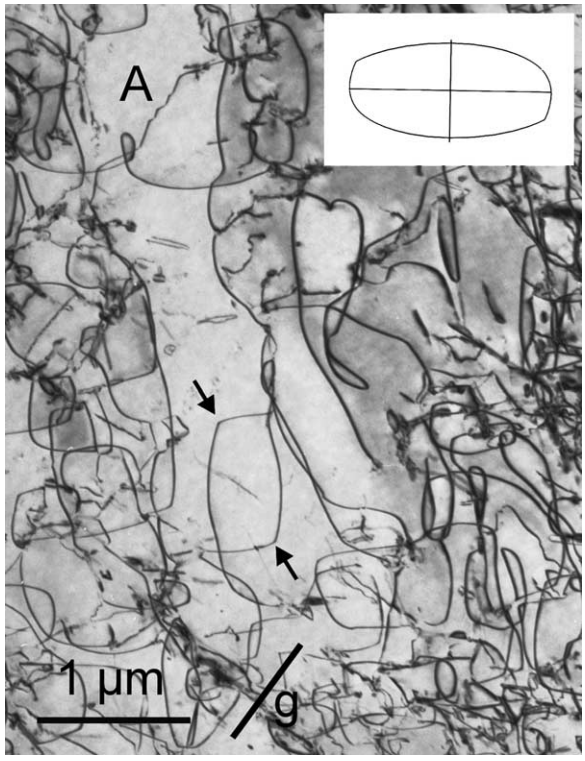

Fig. 9. Dislocation structure in a foil cut parallel to the (101) primary slip plane of a sample deformed about 0.45% at 495 °C and a strain rate of 10^{-5} s^{-1}. $\mathbf{g}=(020)$ near $\mathbf{n}=[101]$. Inset: elastic equilibrium shape of dislocation with $[11\bar{1}]$ Burgers vector.

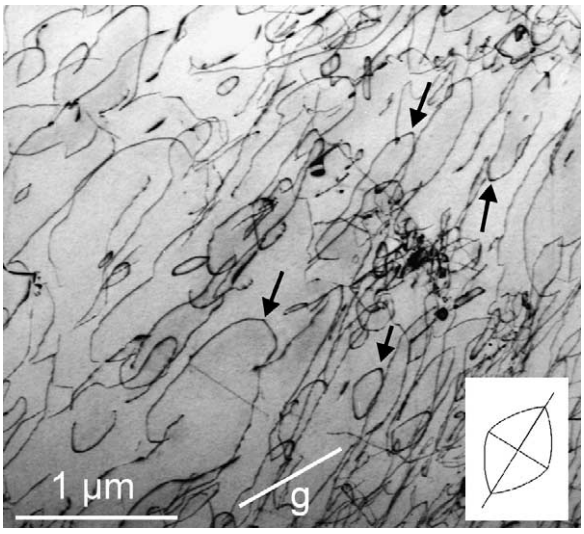

Fig. 10. Dislocation structure in a cross-sectional foil of a sample deformed about 1% at 533 °C at different strain rates followed by about 1.4% at 564 °C, the last 0.5% at a strain rate of $10^{-4}\,s^{-1}$. $\mathbf{g}=(1\bar{1}0)$ near $\mathbf{n}=[111]$. Inset: elastic equilibrium shape of dislocation with [010] Burgers vector projected onto the image plane.

between the obstacles are in the range of 0.1 μm. Video recordings show that the dislocations move in a very jerky way between stable positions. The distance between the stable positions is much larger than the obstacle distance *l*.

In the experiments at higher temperatures, several times a single specimen was deformed successively at different temperatures. The displacement of the straining stage was controlled in such a way that dislocation velocities in the range of about 10–1000 nm s^{-1} were achieved, which can well be recorded. At the in situ tensile stage used, the applied load can be measured. The loads to obtain dislocation velocities in the range mentioned above are plotted in Fig. 12 versus temperature for three in situ experiments. Each symbol

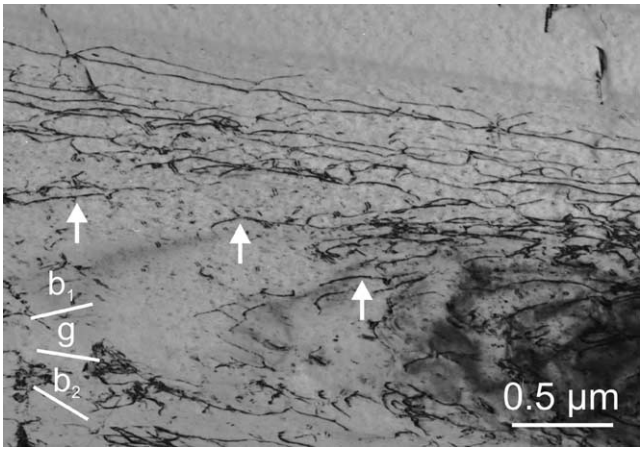

Fig. 11. Dislocations moving during an in situ straining experiment in the HVEM at room temperature. $\mathbf{g}=(10\bar{1})$ near $\mathbf{n}=[1\bar{2}1]$. **g** is parallel to the trace of the (101) primary slip plane. $\mathbf{b}_1$ and $\mathbf{b}_2$ are the projections of the $[11\bar{1}]$ and $[\bar{1}11]$ Burgers vectors onto the image plane.

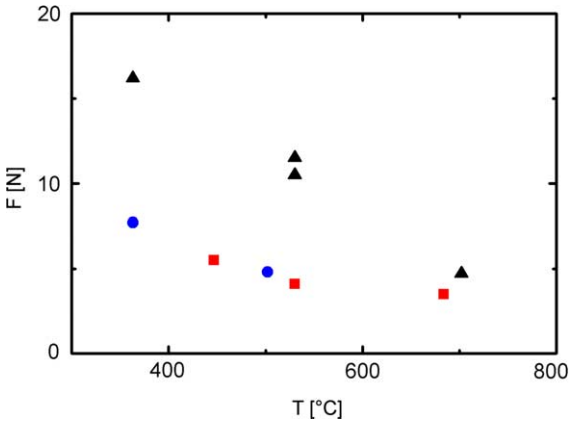

Fig. 12. Dependence of the load to achieve dislocation velocities in the range of 10–1000 nm s^{-1} on the temperature during in situ straining experiments with temperature changes. Three individual experiments are indicated by different symbols.

corresponds to one specimen deformed at different temperatures. In all experiments, there is a continuous decrease of the loads with increasing temperature, i.e. the anomalous increase of the flow stress did not occur during the in situ tests.

At 363 °C, the slip traces are straight and belong to glide on (101) and (011) planes, with cross slip events between both planes as demonstrated at the left side of Fig. 13. The dislocations at the ends of the slip traces consist of straight segments in two orientations. One orientation is the projection of the screw direction of dislocations with $[11\bar{1}]$ Burgers

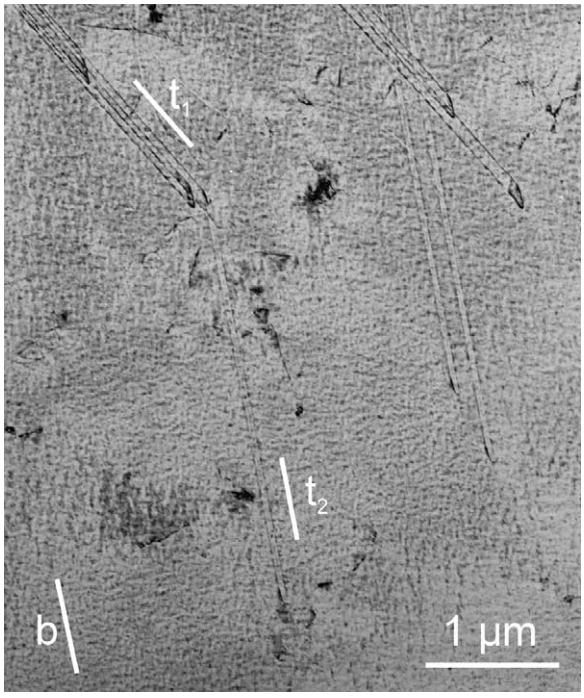

Fig. 13. Traces $\mathbf{t}_1=[10\bar{1}]$ of (101) and $\mathbf{t}_2=[31\bar{1}]$ of (011) slip planes (thin long lines) and dislocations (thick lines at the ends of the traces) moving during in situ straining at 363 °C. $\mathbf{g}=(10\bar{1})$, $\mathbf{n}=[1\bar{2}1]$. **b** is the projection of the $[11\bar{1}]$ Burgers vector.

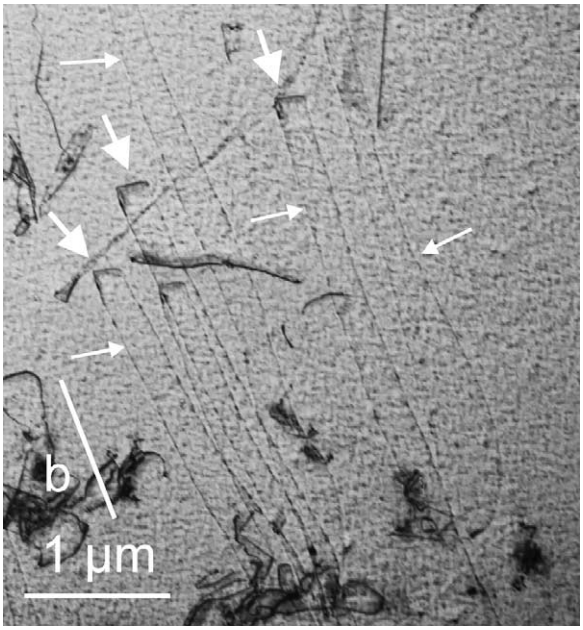

Fig. 14. Slip traces and dislocations moving slowly during in situ straining in an HVEM at 530 °C. $\mathbf{g} = (10\bar{1})$, $\mathbf{n} = [1\bar{2}1]$.

vectors. The other one corresponds to a mixed orientation with a large edge component, which may be $[\bar{1}11]$ on the (101) plane. Fig. 14 was taken at 530 °C, i.e. in the anomaly range of macroscopic deformation tests. Here, the slip traces (thin arrows) are curved pointing at the superposition of climb or cross slip in addition to glide. Nevertheless, the traces are close to those of the (011) planes. The dislocations (thick arrows) imaged with the $(10\bar{1})$ reflections belong to the primary $[11\bar{1}]$ Burgers vectors. They move very slowly in a viscous way and exhibit straight segments. One of the projections is again consistent with the screw orientation. The other projection is close to the [012] direction. It may correspond to a 60° dislocation on the (011) plane.

In addition, slip bands occur with dislocations, which are extinguished at $\mathbf{g} = (10\bar{1})$. These dislocations were imaged with a (211) $\mathbf{g}$ vector at the $[1\bar{3}1]$ pole as demonstrated in Fig. 15 taken at 447 °C. They are also invisible at $\mathbf{g} = (200)$ so that their Burgers vector is [010]. The orientation of the slip traces suggests again (101) slip planes. These dislocations are straight with the projections corresponding to ⟨111⟩ directions, i.e. the angle between the Burgers vectors and the dislocation lines is 54.7°. These dislocations move also in a viscous way but much faster than the dislocations with $[11\bar{1}]$ Burgers vectors. After unloading, they relax into a curved shape. The dislocations with [010] Burgers vectors move and multiply in bands separated from the bands with ⟨111⟩ dislocations, i.e. they are not formed by decomposition of the latter.

At high temperatures (685, 700 °C), smoothly curved dislocations move viscously in a very irregular way pointing at a combination of glide with rapid climb. New dislocation length is created continuously by bowing of certain segments. On the other hand, frequently dislocation segments coming across each other annihilate, so that the dislocation density

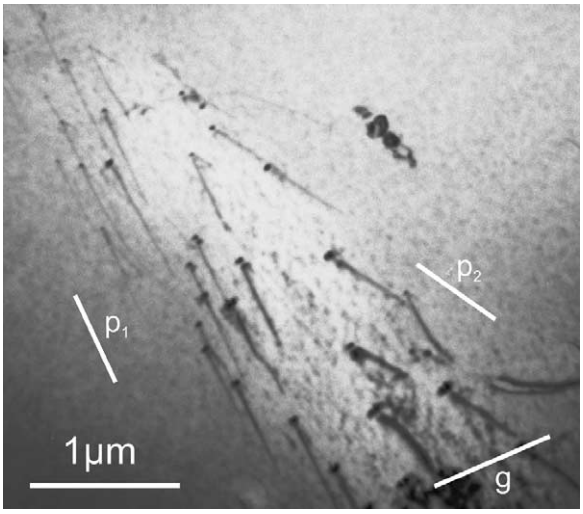

Fig. 15. Dislocations moving during in situ straining at 447 °C. $\mathbf{g} = (112)$, $\mathbf{n} = [1\bar{3}1]$. Projections $\mathbf{p}_1 = [71\bar{4}]$ of $[\bar{1}11]$ direction and $\mathbf{p}_2 = [\bar{4}17]$ of $[11\bar{1}]$ direction.

keeps on a low level over a long time of observation. Fig. 16 presents an example of the creation and shrinkage of a dislocation loop. In the frame taken at 0 s, a moving dislocation is marked by four thin arrows. Since the dislocation moves fast, its image is blurred. Between the frame at 0 s and the following one at 1.24 s a dislocation loop labelled by the thick arrow is created. In the following frames, the loop shrinks and has disappeared in the last frame taken at 3.04 s. When the dislocations stop moving, they form straight segments, the projections of which are consistent with the three ⟨100⟩ line directions.

4. Discussion

4.1. Elastic properties of dislocations

Some features of the dislocation microstructures are controlled by the elastic properties of the dislocations. Using anisotropic elasticity theory, dislocation energies were first calculated for screw and edge dislocations in B2 Fe–Al of different composition [21]. A comprehensive study of the elastic properties of dislocations with all relevant Burgers vectors in B2 Fe–Al of different composition is given in [22]. According to that, dislocations with ⟨111⟩ and ⟨100⟩ Burgers vectors are elastically unstable in certain orientation ranges. To interpret the shape of dislocations with cusps in Figs. 9 and 10, dislocation line energies E and line tensions $T = E + \mathrm{d}^2E/\mathrm{d}\phi^2$ were re-calculated on the basis of the line tension model in anisotropic elasticity, using a PC program [23]. ϕ is the angle between the Burgers vector and the orientation of the dislocation line. Elastic constants were taken from [24]. Calculated shapes of dislocation loops in elastic equilibrium on the (101) plane are plotted in the insets of Figs. 9 and 10 for the $[11\bar{1}]$ and [010] Burgers vectors. The line tension maxima and minima of the ⟨111⟩ dislocation are not located at the screw and edge orientations and differ by a factor of about 8, resulting in the elongated shape of the equilibrium loop. Between about

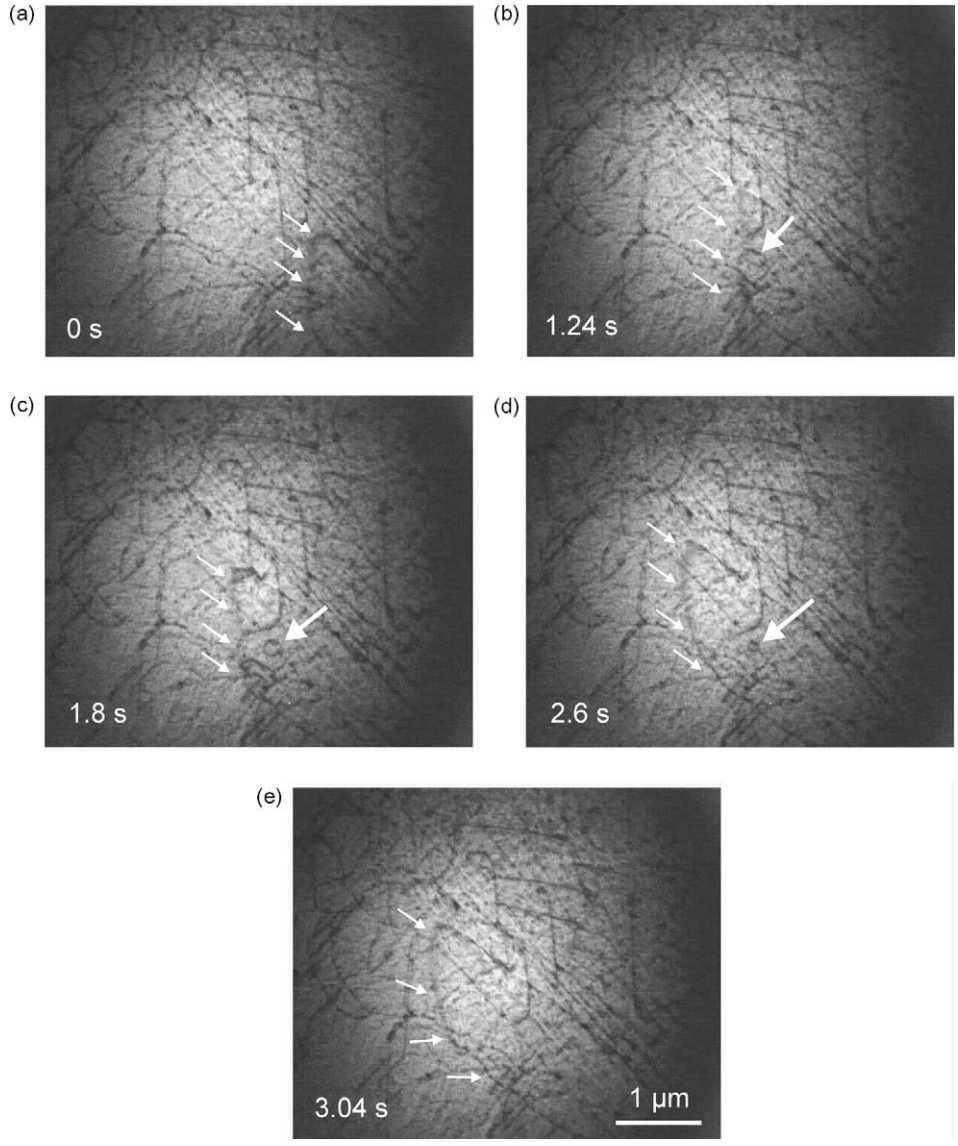

Fig. 16. Section of a video recording taken at 702 °C showing the formation and shrinkage of a dislocation loop. $\mathbf{g} = (10\bar{1})$, $\mathbf{n} = [1\bar{2}1]$.

38 and 55°, i.e. for orientations close to $[10\bar{1}]$, the dislocations are unstable resulting in edges in the dislocation line. The edges in the dislocation lines and preferential orientations are visible in Fig. 9. As stated in [22], the edges in dislocations with ⟨111⟩ Burgers vectors have not clearly been evidenced before.

The energy of the [010] dislocation shows an anomalous decrease with increasing edge character with the minimum at about 125°. The shape of this dislocation is symmetric around the Burgers vector direction with relatively flat segments at the two ⟨111⟩ orientations. The screw orientation is unstable in the range between about −14 and 14°. The instability of the screw direction and the preferential orientations are visible in Fig. 10, which shows also many mixed dislocations, which decomposed into straight segments. Apparently, the edge orientation seems to be another preferential orientation, which is not described by the elastic dislocation properties. While the line tension properties influence the shape of dislocations in the unloaded configuration, they seem not to be responsible for the straight shape of dislocations during their motion in the in situ experiments as described below.

The following discussion of the processes controlling the deformation is divided according to three temperature ranges, room temperature, the range of the flow stress anomaly and the range above the peak temperature.

4.2. Room temperature

In situ straining experiments show dislocations with ⟨111⟩ Burgers vectors slightly bowing between obstacles of an average distance of $l \cong 0.1$ μm (Fig. 11) and moving in a jerky way. This is a mechanism typical of low temperatures also in other intermetallic alloys (e.g. TiAl [25]). Whether the obstacles are jogs or small precipitates was not studied further.

In situ straining experiments at room temperature were already performed before with similar results [26].

At room temperature, the stress relaxation curves are bent towards the stress axis in the normal way (Fig. 5). The strain rate sensitivity of $r=2.6$ MPa at $\dot{\varepsilon}=10^{-5}\,s^{-1}$ (Fig. 6) is related to the so-called activation volume V by

$$V = kT/(m_s r). \tag{2}$$

k is Boltzmann's constant, T the absolute temperature, and m_s the orientation factor. Eq. (2) yields $V\cong 3.7\times10^{-27}\,m^3$. In microscopic terms, the activation volume is given by

$$V = lbd. \tag{3}$$

Here, l is the obstacle distance as in Section 3.3. with $l\cong 0.1$ μm, b the absolute value of the Burgers vector ($b_{\langle 111\rangle}=0.498$ nm), and d the so-called activation distance, an effective diameter of the obstacles at the stress applied. With the data above, it follows that $d\cong 0.15b$. This is a usual value for dislocation motion controlled by localized obstacles like small precipitates. The very jerky motion over large distances indicates that the dislocation motion is quite of athermal nature, i.e. that the Peierls mechanism, which frequently acts at low temperatures, is not important.

4.3. Temperature range of the flow stress anomaly

Since macroscopic deformation between room temperature and the peak temperature is carried by dislocations with the $[11\bar{1}]$ Burgers vector (Section 3.2), these dislocations must be responsible for the flow stress anomaly. They move in a viscous way, which contradicts all pinning/unpinning mechanisms with jerky dislocation motion. The anomalous increase of the flow stress must then result from other processes, which additionally impede the motion of these dislocations.

From the literature, it is obvious that point defects play an essential role in the deformation of FeAl at high temperatures, e.g. the structural defects originating from deviations from stoichiometry [27]. The effects of thermal vacancies are recognized in the vacancy hardening model of George and Baker [1], already mentioned in the Introduction, and in other related papers [28,29]. In this model, individual thermal vacancies appearing in the range of the flow stress anomaly are supposed to pin the dislocations as localized non-diffusing obstacles to be treated with the theory of solution hardening. There are several experimental observations supporting the importance of thermal vacancies in connection with the flow stress anomaly. In experiments with fast up heating to the deformation temperature, the flow stress anomaly occurs only after an incubation time in the order of some minutes. This time equals the time necessary to establish the equilibrium concentration of thermal vacancies [30]. Besides, after quenching down from temperatures in the anomaly range, the specimens show the same flow stress at room temperature as those deformed at the annealing temperatures [29]. However, vacancies should not act as fixed localized obstacles at the high temperatures in the range of the anomalous increase of the flow stress as discussed below.

It is difficult to estimate the interaction strength between a vacancy and a dislocation. Considering the vacancy as an inclusion of zero bulk modulus, the maximum interaction energy is given by (see, e.g. [31])

$$\Delta G_0 = \frac{9K_e v}{16\pi^2}\,\frac{1+\nu}{1-\nu}, \tag{4}$$

where v is the volume of the vacancy taken as $v=a^3/2$ with the lattice constant $a=0.288$ nm, and ν is Poisson's ratio ($\nu=0.384$ [32]). K_e is the energy factor of the edge dislocation with $\langle 111\rangle$ Burgers vector on the $\{110\}$ plane. It is taken here instead of the shear modulus. K_e is calculated by the PC programme [23] using the elastic constants from [24] mentioned above. With these data, $K_e=108$ GPa and $\Delta G_0=1.03$ eV. This is a relatively large interaction energy. Assuming, for simplicity, a triangular interaction profile of the width of the absolute value of the Burgers vector, the resulting maximum force is given by

$$F_0 \cong \Delta G_0/(0.5b). \tag{5}$$

This yields $F_0=6.6\times10^{-10}$ N. Based on the arguments in [33], it can be shown that the vacancies are relatively strong obstacles. At the low concentration of $c\cong 3\times10^{-4}$ at the flow stress peak [34], Friedel statistics can be applied. Then, the contribution of the obstacles to the flow stress at zero temperature is given by [35]

$$\sigma_0^* = \frac{0.95}{m_s}F_0^{3/2}\frac{b}{l_{sq}}\frac{1}{\sqrt{2\Gamma b^4}}. \tag{6}$$

l_{sq} is the edge length of a square in the slip plane containing one obstacle. It is set equal to $ac^{-1/2}/2$. Thus, $\sigma_0^*=170$ MPa with the orientation factor $m_s=0.44$ for the $(101)[11\bar{1}]$ slip system. In terms of the Friedel model, the contribution of solution hardening to the flow stress shows strong temperature dependence with a limiting temperature

$$T_0 = \frac{\Delta G_0}{k\ln(\dot{\varepsilon}_0/\dot{\varepsilon})}, \tag{7}$$

above which the contribution is small. k is again Boltzmann's constant, $\dot{\varepsilon}$ the strain rate and $\dot{\varepsilon}_o$ the pre-exponential factor in an Arrhenius equation of the strain rate.[1] With a characteristic value of $\ln(\dot{\varepsilon}_0/\dot{\varepsilon})\cong 25$, T_0 becomes about 200 °C. Consequently, vacancies of the estimated concentration may contribute to the flow stress at low temperatures, e.g. quenched-in vacancies at room temperature, but they should not cause the flow stress anomaly at much higher temperatures.

Several experimental results can well be interpreted by dynamic strain ageing. Effects of strain ageing were observed in FeAl in a number of experiments (e.g. [36–38]) but not in all. In the present study, this concerns in particular the occurrence of the flow stress anomaly itself, the inverse behaviour of the strain rate sensitivity, and the appearance of serrated yielding connected with slip localization. According to [37], serrated

[1] The pre-exponential factor is approximately given by $\dot{\varepsilon}_0 = m_s\rho b\Delta l\nu_0$, where ρ is the (mobile) dislocation density ($\cong 10^{13}\,m^{-2}$), ν_0 an attempt frequency ($\cong 10^{12}\,s^{-1}$), and Δl the jump distance after successful thermal activation with $\Delta l\cong b/\sqrt{c}(\cong 2\times10-8\mathrm{m})$.

yielding depends on the orientation of the loading axis. The present orientation is in the range of unstable slip. Serrated yielding is certainly favoured in single crystals in single slip orientation where slip localization is promoted, as in this study. It is also supported in a stiff testing machine (Section 2). There, sudden strain increments cause large stress drops. In the classical theory of deformation instabilities [18,39,40], so-called strain rate softening instabilities require negative strain rate sensitivity. However, taking into account also collective dislocation processes [41], it is sufficient if the strain rate sensitivity is small, which is fulfilled in the present experiments. The maximum contribution σ^*_{max} of strain ageing to the flow stress (see Fig. 1) and the necessary diffusion coefficient can be estimated using the theory of the Cottrell effect as it is described in [42] and by assuming that the diffusing defects are the Fe vacancies. The maximum stress contribution is given by

$$\sigma_{max} = \frac{17c\beta}{m_s b^4}, \tag{8}$$

where β is the strength of the obstacles. For solutes ([42], Eq. (14–47)),

$$\beta = \frac{\mu b}{3\pi}\frac{1+\nu}{1-\nu}(v_s - v_m). \tag{9}$$

μ is the shear modulus and v_s and v_m are the atomic volumes of the solute and matrix atoms. By comparing this with Eq. (14-42) of [42], it may be concluded that for vacancies

$$\beta = \frac{\mu b}{3\pi}\frac{1+\nu}{1-\nu}v_{rel}, \tag{10}$$

with v_{rel} being the relaxation volume of the vacancy. Since it is not known, it is assumed that it amounts to 30% of the atomic volume, i.e. $v_{rel}=0.3a^3/2$. Using again K_e instead of the shear modulus, the maximum flow stress contribution is only $\sigma^*_{max}=8.6$ MPa. The diffusion coefficient D necessary to obtain the flow stress maximum at a specific temperature T_{max} and strain rate $\dot{\varepsilon}_{max}$ is given by

$$D = \frac{\dot{\varepsilon}_{max}\beta}{4\rho b k T_{max}}. \tag{11}$$

ρ is the dislocation density. A characteristic value in the anomaly range is $\rho=2\times10^{13}$ m^{-2}. With $\dot{\varepsilon}_{max}=10^{-5}$ s^{-1} and $T_{max}=550$ °C, the necessary diffusion coefficient becomes $D=10^{-19}$ m^2 s^{-1}. This is exactly the Fe self-diffusion coefficient at 550 °C [43]. Thus, dynamic strain ageing can qualitatively interpret the dynamic deformation properties, it is consistent with the diffusion coefficient of Fe vacancies but it fails to describe the amount of the anomalous flow stress increase.

Dynamic strain ageing does also not explain the straight crystallographic shape of the dislocations moving during the in situ experiments (Figs. 13 and 14). It was shown in Section 4.2 that the Peierls mechanism might act below room temperature. Nevertheless, the straight arrangement of the moving dislocations is obviously a property of the dislocation cores. There exist only a few theoretical studies of the dislocation core configurations in FeAl (e.g. [44–46]). They suggest that dislocations with both ⟨111⟩ and ⟨100⟩ Burgers vectors dissociate into partial dislocations with Burgers vectors close to 1/2⟨111⟩ which, however, slightly point out of the {110} slip plane. Thus, these dislocations cannot move conservatively in the dissociated configuration. The critical stresses to move the dislocations on {110} planes at zero temperature are between 8 and 320 MPa and are very different for screw and edge dislocations, each, but it seems that these values are not relevant for the dislocation motion in the range of the flow stress anomaly.

In the present paper, it is suggested to explain the straight crystallographically oriented shape of dislocations by a decomposition model originally proposed in [47,48] for the motion of dislocations with ⟨110⟩ Burgers vectors during deformation of NiAl single crystals in the hard ⟨100⟩ orientation. These dislocations are aligned along ⟨111⟩ and edge orientations and decompose according to

$$[110] = [100] + [010]. \tag{12}$$

The decomposition takes place along the preferential directions by glide on low index planes. The component dislocations cannot glide on the slip plane of the total dislocation. The motion of the total dislocation occurs by a combination of glide of the components on their slip planes and so-called conservative climb, i.e. a flux of point defects from one component dislocation to the other one. The necessity of climb allows the motion of the total dislocation only at high temperatures. The flux of the generated vacancies is automatically equal to the flux of absorbed vacancies as long as the total dislocation moves on its slip plane. The preferential orientations are the intersection lines of the low index slip planes of both the total dislocation and their components. The proposed model is basically different from the climb dissociation model [5], which was applied to FeAl in [4], where the dislocations dissociate by climb and have to constrict before they move. The strong alignment of dislocations with ⟨110⟩ Burgers vectors along ⟨111⟩ in NiAl was also observed during dislocation motion in in situ straining experiments [49]. It has been suggested that the decomposition model is also responsible for the motion of straight dislocations in $MoSi_2$ single crystals at high temperatures [15,50].

In FeAl, the preferential orientations of the dislocations during motion are almost all of the type ⟨111⟩, i.e. the screw orientation and a mixed orientation for dislocations with $[11\bar{1}]$ Burgers vectors as well as a mixed orientation for the ⟨100⟩ dislocations. Only the case of the ⟨111⟩ screw dislocation was treated in the core structure calculations in [44–46]. Possible decomposition schemes in analogy to the model for NiAl are listed in Table 2. According to that, the screw dislocation on a (101) plane with a $[11\bar{1}]$ Burgers vector can decompose by glide into three components with complete ⟨100⟩ Burgers vectors

$$[11\bar{1}](101) = [100](0\bar{1}\,\bar{1}) + [010](101) + [00\bar{1}](\bar{1}10) \tag{13}$$

(reaction 1 in Table 2). All the involved slip planes are of the type {110}, which seems to be the preferred slip plane in FeAl.

Table 2
Decomposition of dislocations with ⟨111⟩ Burgers vectors in FeAl

Reaction	Total dislocation			Component dislocations			Energy gain $E_T - \Sigma E_c$ $[10^{-9}$ N]
	Line orientation, ϕ	Burgers vector	E_T $[10^{-9}$ N]	Burgers vector	Plane, ϕ	E_c $[10^{-9}$ N]	
1	$[11\bar{1}]$, 0°	$[11\bar{1}]$	1.005	[100]	$(0\bar{1}\bar{1})$, 54.7°	0.593	
				[010]	(101), 54.7°	0.593	
				$[00\bar{1}]$	$(\bar{1}10)$, 54.7°	0.593	-0.774
2	$[\bar{1}11]$, 109,5°	$[11\bar{1}]$	2.039	[100]	$(01\bar{1})$, 125.3°	0.593	
				[010]	(101), 54.7°	0.593	
				$[00\bar{1}]$	(110), 125.3°	0.593	0.26

The slip plane of the second component is the same as that of the total dislocation so that this component can move by glide. The two other components have to move by a combination of glide and conservative climb as discussed above. Table 2 lists also the character ϕ of all dislocations. The energy E_T of the starting dislocation and the energies of the components E_c on the respective slip planes were calculated again in the framework of anisotropic elasticity theory by the PC programme of [23], where

$$E = \frac{K(\varphi)b^2}{4\pi}, \tag{14}$$

i.e. E is the energy per length of the respective dislocations without consideration of the logarithmic factor. The last column of Table 2 contains the energy gain by the reactions. It is strongly negative for the considered reaction 1 (Eq. (13)) so that this reaction is not driven by the long-range stress field. Nevertheless, it may occur owing to a special core configuration although this reaction is not suggested by the calculations in [44–46]. On the other hand, the near-edge dislocation with a $[11\bar{1}]$ Burgers vector with a very high energy can decompose with a considerable gain in elastic energy (reaction 2 in Table 2).

In the original model for NiAl [48], the rate of the vacancy flux between the climbing component dislocations and thus the velocity of the total dislocation is estimated by assuming a constant width of the decomposed dislocation. This leads to monotonously increasing dislocation mobility with increasing temperature. In the present paper, it is suggested to extend the model by considering a possible dependence of the width of the decomposed dislocations on the dislocation velocity and the temperature. Since there does not yet exist a detailed theory of this process, it is assumed that the decomposition width plays a similar role as the width of the diffusing point defect cloud around the dislocations in the theory of the Cottrell effect described above. This dependence results in the dynamic dislocation behaviour of Fig. 1, leading to the occurrence of a flow stress anomaly, the inverse dependence of the strain rate sensitivity on the stain rate or stress and to plastic instabilities, phenomena, which are all observed in the present study. Since both processes, the Cottrell effect and the conservative climb motion of a decomposed dislocation require diffusion processes in the dislocation cores over similar distances, Eq. (11) should give quite a correct estimation of the temperature of the flow stress anomaly. Climb in the dislocation cores in FeAl is quite probable since general climb was observed in the same temperature range.

4.4. High-temperature range

The transition from the range of the flow stress anomaly to the high-temperature range with a strongly decreasing flow stress may be caused by two processes. As first suggested in [9], the dominating Burgers vectors change from $[11\bar{1}]$ to ⟨100⟩. In situ straining experiments had shown that the latter are much more mobile. In addition, recovery processes become important.

In the present in situ straining experiments, there is no indication of the formation of dislocations with ⟨100⟩ Burgers vectors by decomposition of dislocations with ⟨111⟩ Burgers vectors. Instead, the ⟨100⟩ dislocations moved in locally separated bands and were generated within these bands by multiplication. In the in situ experiments, the ⟨100⟩ dislocations are also straight and oriented along ⟨111⟩ directions (Fig. 15), which may partly be due to the line tension. However, the straight shape can also result from dissociation reactions, which are not discussed, in detail.

As described above, general climb of the dislocations takes place already in the range of the flow stress anomaly. In the high-temperature region, in addition to the mode of motion, rapid climb causes very fast recovery so that the dislocation

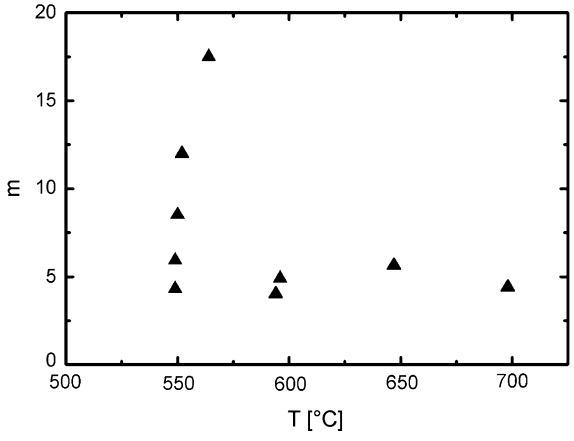

Fig. 17. Dependence of the stress exponent m on the temperature.

density during the in situ straining experiments at 700 °C remains at a low level. As the work hardening is low, the high-temperature deformation can conveniently be treated in terms of an equation for steady state creep (e.g. [51]), as suggested before [1],

$$\dot{\varepsilon}_{ss} = A\frac{\mu b}{kT}\left(\frac{\sigma}{\mu}\right)^{n} D_0 \exp\left(-\frac{\Delta H}{kT}\right), \tag{15}$$

where A is a dimensionless constant, n the stress exponent for creep, D_0 the pre-exponential factor and ΔH the activation enthalpy of the respective diffusion process. Depending on the particular creep model, stress exponents are expected between about 4 and 6. Stress exponents m can also be determined from the strain rate sensitivity r according to

$$m = \mathrm{d}\ln\dot{\varepsilon}/\mathrm{d}\ln\sigma = \sigma/r. \tag{16}$$

They are plotted in Fig. 17 and show a very large scatter at the flow stress peak but are equal to about 5 in the whole high-temperature range. These experimental values of m are well in the range of the theoretical values n for creep. Thus, the strain rate sensitivity data also suggest the importance of recovery during the high-temperature flow stress decrease.

5. Conclusions

- Fe–43at%Al single crystals show a flow stress anomaly accompanied with an inverse dependence of the strain rate sensitivity of the flow stress on the strain rate or the stress in a narrow temperature range.
- Serrated flow occurs up to the flow stress peak.
- In macroscopic tests, the deformation is carried by dislocations with ⟨111⟩ Burgers vectors up to the peak temperature. Above that temperature, dislocations with ⟨100⟩ Burgers vectors dominate.
- Curved slip traces during in situ straining experiments in a high-voltage electron microscope and a non-planar arrangement of dislocations after macroscopic deformation indicate the importance of climb in the range of the flow stress anomaly.
- In the in situ experiments, viscously moving dislocations are straight and crystallographically oriented.
- The phenomena listed above are interpreted by a decomposition of the cores of the dislocations with ⟨111⟩ Burgers vectors into three component dislocations with ⟨100⟩ Burgers vectors where, similar to a model by Mills et al., two of the component dislocations have to move by a combination of glide and conservative climb.
- This model can be extended by considering a dependence of the decomposition width on the temperature and the dislocation velocity resulting in a dynamic behaviour like the Cottrell effect and causing dynamic strain ageing.

Acknowledgements

The authors are grateful to Dr E.P. George (Oak Ridge National Laboratory) for supplying the single crystals for this study and for fruitful discussions. They also thank Rosamunde Möhner for technical help and the Deutsche Forschungsgemeinschaft for financial support.

References

[1] George EP, Baker I. A model for the yield strength anomaly of Fe–Al. Philos Mag A 1998;77:737–50.
[2] Umakoshi Y, Yamaguchi M, Namba Y, Murakami M. The effect of crystal orientation on the strength anomaly in β CuZn at around 200 °C. Acta Metall 1976;24:89–93.
[3] Yoshimi K, Hanada S. In: Dariola R, Lewandowski JJ, Liu CT, Martin PL, Miracle DB, Nathal MV, editors. Structural intermetallics. Warrendale, PA: Metallurgical Society of AIME; 1993. p. 475.
[4] Morris DG. The yield stress anomaly in FeAl: alloys: the local climb lock model. Philos Mag A 1995;71:1281–94.
[5] Saka H, Zhu YM. Climb dissociation of ⟨111⟩ superdisloctions in β CuZn. Philos Mag A 1985;51:629–37.
[6] Carleton RL, George EP, Zee RH. Effects of deviations from stoichiometry on the strength anomaly and fracture behaviour of B-doped FeAl. Intermetallics 1995;3:433–41.
[7] Baker I, Gaydosh DJ. Flow and fracture of Fe–Al. Mater Sci Eng 1987;96:147–58.
[8] Umakoshi Y, Yamaguchi M. Deformation of FeAl single crystals at high temperatures. Philos Mag A 1980;41:573–88.
[9] Xiao H, Baker I. The temperature dependence of the flow and fracture of Fe–40Al. Scripta Metall Mater 1993;28:1411–6.
[10] Kad BK, Horton JA. Discrepancies between microscopic (TEM) and macroscopic (texture) observations in high temperature deformation of FeAl and Fe_3Al-based alloys. Mater Sci Eng A 1997;239–240:118–25.
[11] Yoshimi K, Yoo MH, Hanada S. Slip band propagation and slip vector transition in B2 FeAl single crystals. Acta Mater 1998;46:5769–76.
[12] Molénat G, Couret A, Caillard D. Peierls friction stresses and dynamic strain ageing in TiAl and Fe–30at.% Al alloys. Mater Sci Eng A 1997;234–236:660–3.
[13] Cottrell AH. A note on the Portevin–LeChatelier effect. Philos Mag 1953;74:829–32.
[14] Messerschmidt U, Bartsch M, Guder S, Häussler D. Dislocation dynamics during the deformation of intermetallic alloys and the flow stress anomaly. Mater Res Soc Symp Proc 1999;552:KK10.9.1–KK10.9.6.
[15] Messerschmidt U, Guder S, Häussler D, Bartsch M. Dislocation dynamics in intermetallic and oxide dispersion strengthened (ODS) alloys. Mater Res Soc Symp Proc 2001;652:Y11.6.1–Y11.6.11.
[16] LeChâtelier MA. Rev Métall 1909;6:914.
[17] Portevin A, LeChâtelier F. Comp Rend Sci Paris 1923;176:507.
[18] Kubin LP, Estrin Y. A nonlinear aspect of crystal plasticity—The Portevin–LeChatelier effect. J Phys (Paris) 1986;47:497–506.
[19] Messerschmidt U, Appel F. Quatitative tensile-tilting stages for the high voltage electron microscope. Ultramicroscopy 1976;1:223–30.
[20] Messerschmidt U, Bartsch M. High-temperature straining stage for in situ experiments in the high-voltage electron microscope. Ultramicroscopy 1994;56:163–71.
[21] Mendiratta MG, Law CC. Dislocation energies and mobilities in B2-ordered Fe–Al alloys. J Mater Sci 1987;22:607–11.
[22] Yoo MH, Yoshimi K, Hanada S. Dislocation stability and deformation mechanisms in iron aluminides and silicide. Acta Mater 1999;47:3579–88.
[23] Baither D. PC code for calculating dislocation line energies and tensions in anisotropic elasticity theory. Information by D. Baither, Metal Physics, Münster University; 1999. e-mail: baither@uni-muenster.de.
[24] Leamy HJ, Gibson ED, Kayser FX. Elastic stiffness coefficients of iron–aluminium alloys. I. Experimental results and thermodynamic analysis. Acta Metall 1967;15:1827.
[25] Häussler D, Bartsch M, Aindow M, Jones IP, Messerschmidt U. Dislocation processes during the plastic deformation of γ-TiAl. Philos Mag A 1999;79:1045–71.

[26] Baker I, Horton JA. In situ straining of FeAl in a transmission electron-microscope. Philos Mag A 1993;67:479–89.
[27] Reimann U, Sauthoff G. Effects of deviations from stoichiometry on the deformation behaviour of FeAl at intermediate temperatures. Intermetallics 1999;7:437–45.
[28] George EP, Baker I. Thermal vacancies and the yield anomaly of FeAl. Intermetallics 1998;6:759–63.
[29] Morris DG, Liu CT, George EP. Pinning of dislocations and the origin of the stress anomaly in FeAl alloys. Intermetallics 1999;7:1059–68.
[30] Schaefer H-E, Damson B, Weller M, Arzt E, George EP. Thermal vacancies and high-temperature mechanical properties of FeAl. Phys Status Solidi A 1997;160:531–40.
[31] Friedel J. Dislocations. Oxford: Pergamon Press; 1964. p. 364.
[32] Yoo MH, Takasugi T, Hanada S, Izumi O. Slip modes in B2-type intermetallic alloys. Mater Trans JIM 1990;31:435–42.
[33] Labusch R, Schwarz R. Simulation of thermally activated dislocation motion in alloys. In: Brandon DG, Chaim R, Rosen A, editors. Strength of metals and alloys. London: Freund Publications; 1991. p. 47–68.
[34] Schaefer H-E, Badura-Gergen K. Systematics of thermal defect formation, migration and of self-diffusion in intermetallic compounds. Defect Diffus Forum 1997;143–147:193–208.
[35] Neuhäuser H, Schwink C. Solid solution strengthening. In: Mughrabi H, editor. Plastic deformation and fracture of materials, materials science and technology, vol. 6. Weinheim: VCH; 1993. p. 191–250.
[36] Morris DG, Joyce JC, Lebeouf M. Hardening and strain aging by vacancies and their aggregates in FeAl. Philos Mag A 1994;69:961–80.
[37] Yoshimi K, Hanada S, Yoo MH. Yielding and plastic flow behavior of the B2-type Fe–39.5mol%Al single crystals in compression. Acta Metall Mater 1995;43:4141–51.
[38] Briguet C, Morris DG. Unloading yield point effects in iron aluminides. Acta Mater 1998;46:5053–61.
[39] Kubin LP, Chihab K, Estrin Y. The rate dependence of the Portevoin–Le Chatelier effect. Acta Metall 1988;36:2707–27.
[40] Kubin LP, Estrin Y. Evolution of dislocation densities and the critical conditions for the Portevin–Le Chatelier effect. Acta Metall Mater 1990; 38:697–708.
[41] Zaiser M, Hähner P. Oscillatory modes of plastic deformation: theoretical concepts. Phys Status Solidi B 1997;199:267–330.
[42] Hirth JP, Lothe J. Theory of dislocations. New York: Wiley; 1982.
[43] Eggersmann M, Mehrer H. Diffusion in intermetallic phases of the Fe–Al system. Philos Mag A 2000;80:1219–44.
[44] Vailhe C, Farkas D. Trends in dislocation core structures and mechanical behavior in B2 aluminides. Mater Res Soc Symp Proc 1995;364:395–401.
[45] Vailhe C, Farkas D. Shear faults and dislocation core structure simulations in B2 FeAl. Acta Mater 1997;45:4463–73.
[46] Vailhe C, Farkas D. Transition from dislocation core spreading to dislocation dissociation in a series of B2 compounds. Philos Mag A 1999; 79:921–31.
[47] Mills MJ, Srinivasan R, Daw MS. Observations and modelling of a⟨011⟩ dislocations in NiAl at intermediate temperatures. Philos Mag A 1998;77: 801.
[48] Srinivasan R, Daw MS, Noebe RD, Mills MJ. Observation of glide and decomposition of a⟨101⟩ dislocations at high temperatures in Ni–Al single crystals deformed along the hard orientation. Philos Mag 2003;83: 1111–35.
[49] Messerschmidt U, Häussler D, Bartsch M, Sauthoff G. Dislocation processes during the deformation of NiAl–0.2at.%Ta. Intermetallics 1999;7:455–66.
[50] Guder S, Bartsch M, Messerschmidt U. Transmission electron microscopy analysis of planar faults on (001) planes in $MoSi_2$ single crystals. Philos Mag A 2002;82:2737–54.
[51] Cannon WR, Langdon TG. Creep of ceramics. 1. Mechanical characteristics. J Mater Sci 1983;18:1–50.